metals

MDPI

Communication

The Tribocorrosion Behavior of High-Nitrogen Bearing Stainless Steel in Acetic Acid at Various Applied Loads

Qiong Su [1,2], Xuhui Wang [1,2,3], Hongling Wang [1,2], Yaqi Huang [1,2,3], Yanbin Wang [1,2,*] and Zhenhua Li [1,2,*]

[1] School of Chemical Engineering, Northwest Minzu University, Lanzhou 730000, China; hgsq@xbmu.edu.cn (Q.S.); y211830616@stu.xbmu.edu.cn (X.W.); wang_hongling@163.com (H.W.); y211830597@stu.xbmu.edu.cn (Y.H.)

[2] Key Laboratory of Environment-Friendly Composite Materials of the State Ethnic Affairs Commission, Gansu Provincial Biomass Function Composites Engineering Research Center, Key Laboratory for Utility of Environment-Friendly Composite Materials and Biomass, University of Gansu Province, Lanzhou 730030, China

[3] State Key Laboratory of Solid Lubrication, Lanzhou Institute of Chemical Physics, Chinese Academy of Sciences, Lanzhou 730000, China

* Correspondence: ybwang@126.com (Y.W.); lizhh02006@xbmu.edu.cn (Z.L.)

Abstract: High-nitrogen stainless steels, which are developed by replacing nickel with nitrogen, have been widely applied in manufacturing wear parts in mechanical engineering. In this study, the tribocorrosion performance of a ferritic high-nitrogen bearing stainless steel (40Cr15Mo2VN) under acetic acid solution with a pH of 3.0 was investigated under different loads ranging from 25 N to 125 N. Quantitative calculations indicated that pure mechanical wear was the predominant cause of material degradation, while the corrosion-accelerated wear component also played a crucial role. The material loss induced by both tribocorrosion and mechanical wear increased with increasing load, leading to severe delamination at sliding surfaces and larger wear debris.

Keywords: 40Cr15Mo2VN; tribocorrosion; synergetic effect; applied loads

check for updates

Citation: Su, Q.; Wang, X.; Wang, H.; Huang, Y.; Wang, Y.; Li, Z. The Tribocorrosion Behavior of High-Nitrogen Bearing Stainless Steel in Acetic Acid at Various Applied Loads. *Metals* **2023**, *13*, 1287. https://doi.org/10.3390/met13071287

Academic Editor: Youngsik Kim

Received: 15 May 2023
Revised: 28 June 2023
Accepted: 3 July 2023
Published: 17 July 2023

1. Introduction

Helicopter structural components are being subjected to the ever-increasing demand for materials with improved performance and safety. However, these structures are inevitably exposed to harsh conditions and continually influenced by high temperature, salt fog and acid rain. For moving components such as bearings or gears, the damage induced by wear, scuffing and debris damage will also lead to premature failure. A comprehensive investigation revealed that scuffing and debris damage due to wear and pitting induced by corrosion account for over 61% of the causes of failure occurring in helicopter structural components [1]. In the case of bearings, as the components most likely to fail, it appears that the majority of failures involve specific low-alloy bearing steels such as SAE 52100.

High-nitrogen stainless steel has become an increasingly important structural material, being widely used in helicopter bearings [2–5]. High-nitrogen stainless steel is widely used in the aerospace, marine, nuclear and other high-end manufacturing industries, and, at the same time, is also expected to play a role in lightweight automobiles, new energy and other fields, as a promising material for the sustainable development of human society [6–8]. Alloying steel with nitrogen has a beneficial effect on mechanical performance, corrosion and fatigue resistance [9]. During the last few decades, the effect of nitrogen in steels on pitting, crevices and general corrosion has been identified [10,11]. The incorporation of nitrogen in steels can not only enhance yield strength, toughness and wear resistance but also improve steel's repassivation ability and resistance against corrosion [12]. Although the effect of nitrogen on general corrosion differs due to the uncontrollable preparation method and experimental conditions, the effect of nitrogen on pitting corrosion and crevice corrosion has been clearly identified [11]. Gavriljudk et al. reported a positive effect of nitrogen on austenitic stainless steels as a consequence of the enhanced thermodynamic stability of a solid solution and thus its much-improved mechanical properties and corrosion resistance [13,14] Similar conclusions have been continually obtained, revealing that nitrogen expands and stabilizes the austenitic-phase region and serves as an interstitial element that improves solid-solution strengthening [15,16].

More recently, the electrochemical corrosion behavior of high-nitrogen stainless steel in aqueous solutions has been addressed [16–18]. The corrosion resistance of all types of austenitic stainless steel generally depends on the bilayer structure of the formed passive film in an aqueous solution. Specifically, passive films of high-nitrogen stainless steel have a double-layer structure of inner metal oxides and outer metal hydroxides depending on the exposed environment [19]. However, the experiments conducted by Qiao et al. revealed that the formed passive films were not stable in acetic acid, and the corrosion behavior was influenced by oxygen content, sulfuric acid concentration and surface roughness [20].

The more difficult aspect of the tribocorrosion behavior is the need to combine the sciences of tribology together with simultaneous corrosion. Current research is focused on tribocorrosion in seawater environments [5,21–23], but less research has been conducted in acidic solutions. M.M. Singh studied the corrosion behavior of mild steel in acetic acid solutions, and the variation in the corrosion rate of mild steel with varying concentrations of acetic acid solution was evaluated and showed a notable resemblance [24]. When corrosion is coupled with mechanical wear, the total material loss is not simply the sum of wear–corrosion synergism [25]. The results for the interaction between corrosion and wear are not consistent; publications referring to both its positive and negative effects, which depend on the steel type and corrosive medium, have been reported [21–23]. For high-nitrogen stainless steel, wear–corrosion and their interaction are not yet fully understood, and limiting the suitable choices for a given application will extend its service life [26,27].

In this study, the tribocorrosion behavior of 40Cr15Mo2VN as a high-nitrogen stainless steel in a corrosive environment was investigated. An accelerated corrosion–wear experimental method was established using acetic acid solution with a pH value of 3.0 as the corrosive medium. The synergy between mechanical wear in the absence of a corrosive medium and corrosion in the absence of wear was determined and discussed. Special attention was given to the microstructural evolution at surfaces under different applied loads, which is imperative to the efficient and safe use of high-nitrogen stainless steel in corrosive conditions.

2. Experiment

2.1. Materials and Solutions

A commercial high-nitrogen stainless-steel 40Cr15Mo2VN was provided by Luoyang LYC Bearing Co., LTD., in China, and its chemical composition is listed in Table 1. Before wear tests, the 40Cr15Mo2VN specimen needed to be machined to the specified ring block-dimensions. The ring block machining requirements were a 54 mm outer diameter, 38 mm inner diameter and 13 mm height. Analytical-grade acetic acid was provided by Lianlong Bohua (Tianjin) Pharmaceutical Chemistry Co., Ltd. (China). The counterpart made of a ceramic Si_3N_4 pin was provided by Dongguan Kezhong Ceramic Co., Ltd. (Dongguan, China) The Si_3N_4 counterpart had dimensions of $\Phi 5.0 \times 15$ mm with a 0.1 mm chamfer and a flat working surface with a radius of 4.80 mm. The corrosive medium was prepared by dissolving acetic acid in deionized water with a constant pH value of 3.0, and the experimental medium used for mechanical wear experiments was deionized water. To achieve as consistent a surface roughness as possible for the experimental samples, 800-grit SiC sandpaper was used for uniform sanding, sanding and ultrasonic cleaning with alcohol, and insulating paint was used for the other sides of the ring block, except for the working surface.

Table 1. The chemical composition of 40Cr15Mo2VN (wt.%).

Element	**C**	**Cr**	**Mo**	**V**	**Mn**	**Si**	**Ni**	**N**	**Fe**
wt.%	0.42	14.6	1.9	0.33	0.4	0.21	0.41	0.18	Bal.

2.2. Tribocorrosion Tests

The tribocorrosion behavior of 40Cr15Mo2VN in acetic acid solution was studied by coupling the vertical universal friction machine MMW-1 with the electrochemical workstation Prinception Versa STAT 3F and selecting a three-pin–disk model. In the equipment construction, 40Cr15Mo2VN rings were used as the working electrode, Pt gauze was used as the counter electrode, and a commercial Ag/AgCl electrode was selected as the reference electrode. A schematic illustration of the tribocorrosion apparatus is presented in Figure 1, for which it was possible to obtain the trend of the real-time electrochemical signal during the experiment.

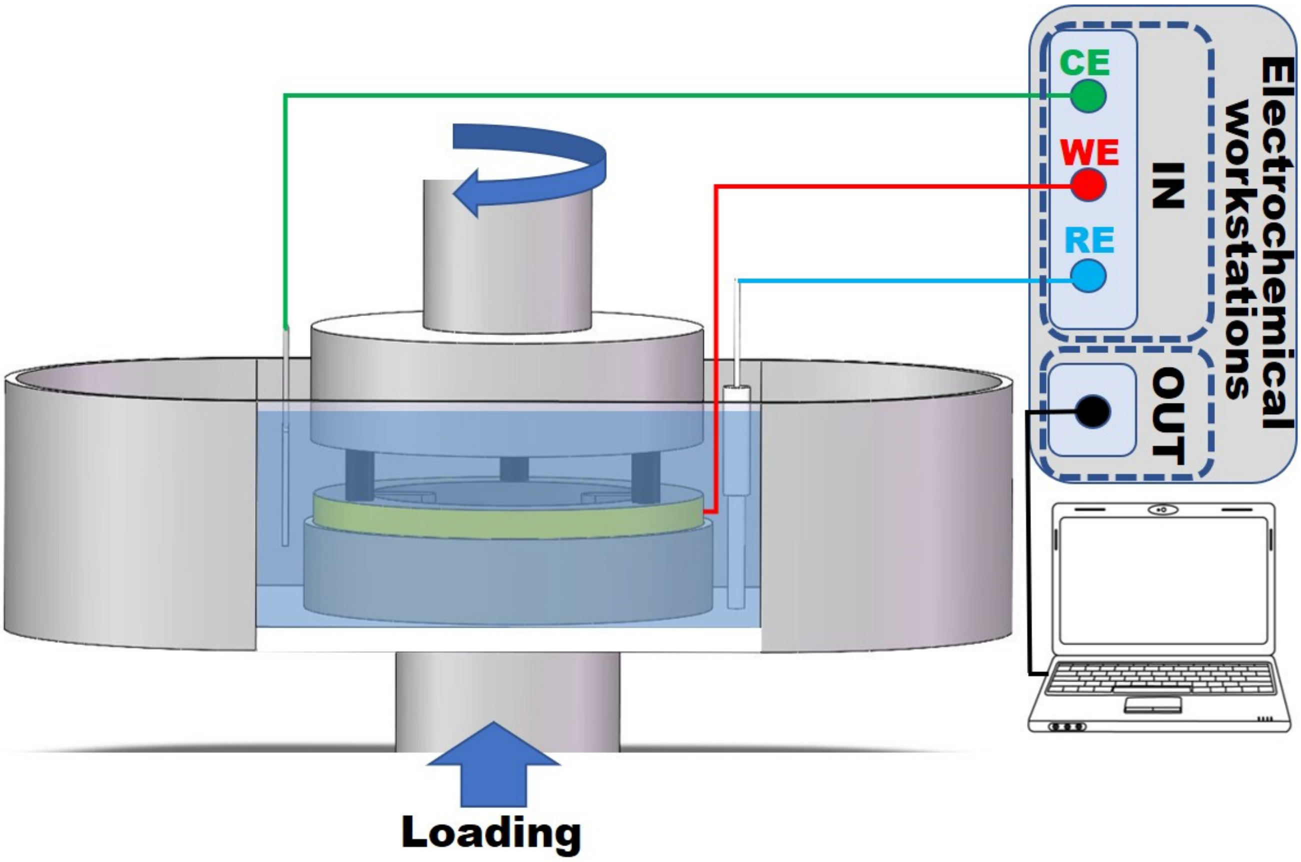

Figure 1. A schematic diagram of the tribocorrosion apparatus.

We conducted tribocorrosion and mechanical wear tests at different loads ranging from 25 N to 125 N with a speed of 120 mm/s for 30 min. The open-circuit potential (OCP) curve was measured at different loads for 5 min with a constant interval of 10 min. The Tafel polarization curves were monitored using a scan rate of 10 mV/s from −0.6 V to 0.3 V in acetic acid solution before and during tribocorrosion tests. Pure mechanical wear was carried out in deionized water.

The interaction between corrosion and mechanical wear was evaluated in accordance with the ASTM G119-09 standard. The total mass loss rate T was calculated according to Equation (1).

$$T = C_0 + W_0 + S \tag{1}$$

where C_0 is the material loss induced by corrosion in the absence of wear, W_0 is the material loss induced by wear in the absence of a corrosive medium, and S is the wear–corrosion synergism.

The components of T, W_0 and C_0 were determined using Equations (2)–(4), respectively.

$$T = \frac{(m_0 - m_2)}{A\rho t} \tag{2}$$

$$W_0 = \frac{(m_0 - m_1)}{A\rho t} \tag{3}$$

where m_0 is the initial sample mass; m_1 is the final mass of the sample tested in deionized water; and m_2 is the final mass of the sample after tribocorrosion. A is the abrasion mark area, which measured 671.0 mm^2 in this experiment, and ρ is the density of 40Cr15Mo2VN, which was 7.704 g/cm^3. t is the test duration.

The corrosion component without wear C_0 and total corrosion component C_w could be calculated based on Equations (4) and (5) [22,23].

$$C_0 = \frac{3.27 \times 10^{-3} \times i_0 \times E_w}{\rho} \tag{4}$$

$$C_w = \frac{3.27 \times 10^{-3} \times i \times E_w}{\rho} \tag{5}$$

where i_0 and i are the corrosion current densities of the static corrosion and tribocorrosion processes, respectively. E_w is the equivalent weight of the alloy, which was 27.92 in this study.

2.3. Characterization

The morphology of the damaged surface and wear debris of 40Cr15Mo2VN were observed with a JEM-5600LV scanning electron microscope (SEM, JEOL Ltd., Tokyo, Japan) with an operating voltage of 200 V, a working distance of 20 mm and a speckle beam current of 20 A. The morphology of 40Cr15Mo2VN was observed using Electron Backscatter Diffraction (EBSD, EDAX Hikari Plus, EDAX Inc., Mahwah, NJ, USA). To obtain an ideal EBSD sample with no residual stress layer, the ion beam treatment was made to be extremely flat, free of abrasive contamination and scratch-free, with little damage to the sample and essentially no deformation layer. A D8 Discover25 high-resolution X-ray diffractometer (XRD, Bruker Corporation, Karlsruhe, Germany) was used to test the metal surface and to obtain the curves, with a scanning angle range of 30–110° and step of 0.02°. The rubbed surface of the worn pin was observed using an OLYMPUS STM6 optical microscope (Olympus Ltd., Tokyo, Japan), and pictures were captured.

3. Results

3.1. Microstructure

Figure 2 shows the crystalline structure of 40Cr15Mo2VN with 0.18 w.t.% nitrogen. The X-ray diffraction pattern of the as-received 40Cr15Mo2VN indicates that its phase composition consisted of only ferrite. Meanwhile, no obvious peaks assigned to austenite or nitride were observed due to the relatively low nitrogen content [28,29] The IPF map further confirms that 40Cr15Mo2VN consisted of equiaxed crystals that exhibited a relatively uniform grain size and aggregation of <110>, <200> and <211> orientations. The average grain size was approximately 10 μm, which is lower than that of typical austenitic high-nitrogen stainless steel [20].

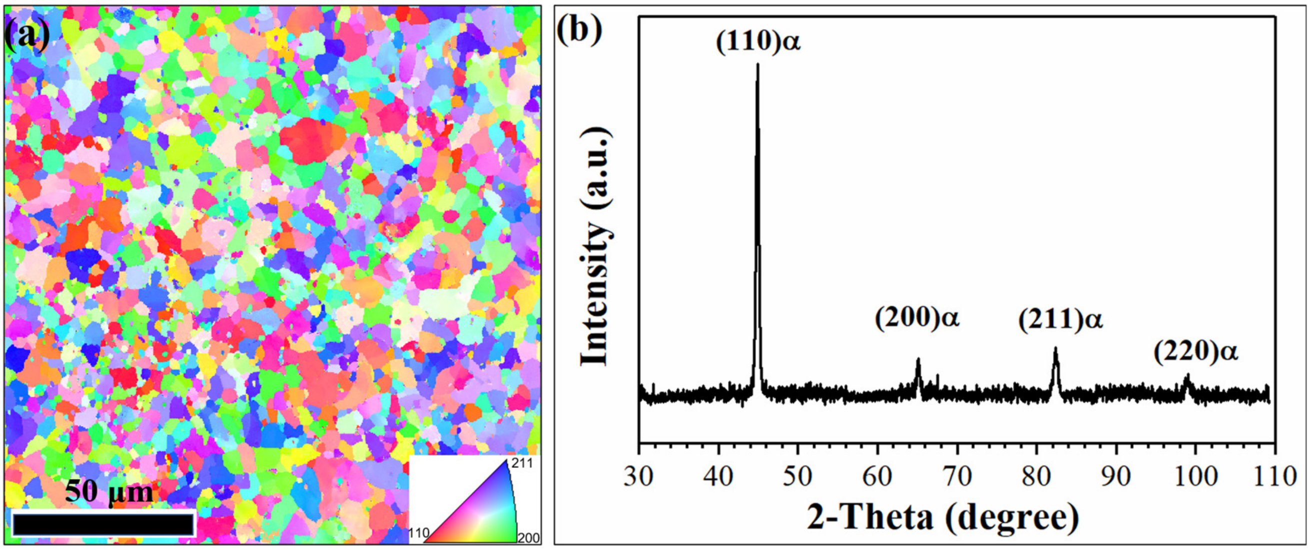

Figure 2. (**a**) The microstructure and (**b**) XRD pattern of 40Cr15Mo2VN.

3.2. Tribocorrosion Behavior

The tribocorrosion behavior of 40Cr15Mo2VN in acetic acid was investigated, and the friction coefficient and material loss rate under different loads are shown in Figure 3. The friction coefficient under both tribocorrosion and mechanical wear increased linearly with increasing load. Typically, the friction coefficient generated by sliding during mechanical wear is higher than that produced during corrosive wear, especially at lower loads. However, the material loss rate under fretting wear was higher than that under mechanical wear, and the difference became more significant as the load increased. When the applied load was 25 N, the wear coefficient in the tribocorrosion condition was 1.9×10^{-4} mm^3/Nm, while the wear coefficient in the mechanical wear condition was slightly lower at 1.6×10^{-4} mm^3/Nm. At 125 N, the wear coefficient induced by tribocorrosion reached 21.9×10^{-4} mm^3/Nm, and the mechanical wear coefficient under the same load was measured as 4.1×10^{-4} mm^3/Nm. That is, the incorporation of simultaneous corrosion promoted wear loss but prevented severe friction.

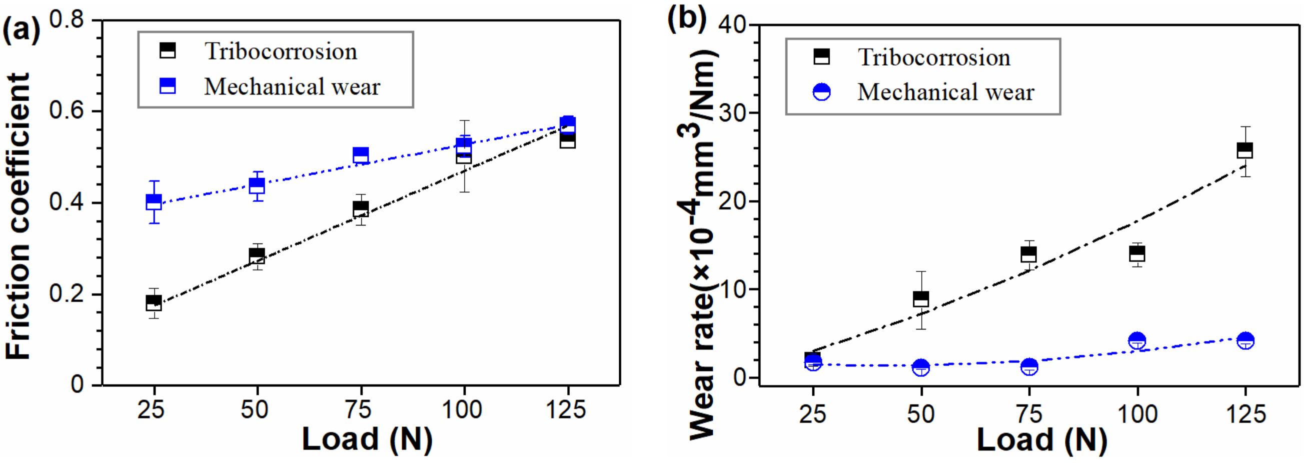

Figure 3. (**a**) Friction coefficient and (**b**) wear rate of 40Cr15Mo2VN under different applied loads in acetic acid solution with a pH value of 3.

The components of corrosion–wear synergism are shown in Figure 4. As can be seen in Figure 4a, the total material loss T mainly consisted of mechanical wear W_0 and corrosion–wear interaction S since the material loss induced by corrosion was negligible, which being typically three orders lower than the values of both W_0 and S. All the material loss components were significantly affected by the applied load. The corrosion–wear interaction showed positive values, illustrating that corrosion produces additional wear. Regarding the synergy in wear components shown in Figure 4b, it is clear that the mechanical wear was accelerated by corrosion, showing a positive value of ΔW_c. At higher loads, the synergy ΔW_c accounted for a larger proportion than mechanical wear W_0 of total wear loss W_c. At 25 N, the value of synergy ΔW_c was measured as 1.4 mm/y, accounting for approximately 6% of the total wear loss W_c of 25.1 mm/y. As the load increased to 125 N, the synergy ΔW_c grew to 1385.4 mm/y, contributing over 83% of the total wear loss W_c. The unit is millimeters per year, which measures the thickness of the material surface that is consumed by corrosion each year. The wear–corrosion components increased at higher loads, showing mutually accelerated wear and corrosion. The total material loss mainly consisted of two parts, namely, pure mechanical wear (W_0) and corrosion-accelerated wear (ΔW_c). For 40Cr15Mo2VN sliding against the harder ceramic counterpart, the mechanical shear and removal became more prominent with increasing load. Then, the fresh surface was exposed to acetic acid, and larger-scale anodic dissolution took place. That is, increased contact stress and accelerated corrosion in the form of anodic dissolution conspired to increase both W_0 and ΔW_c.

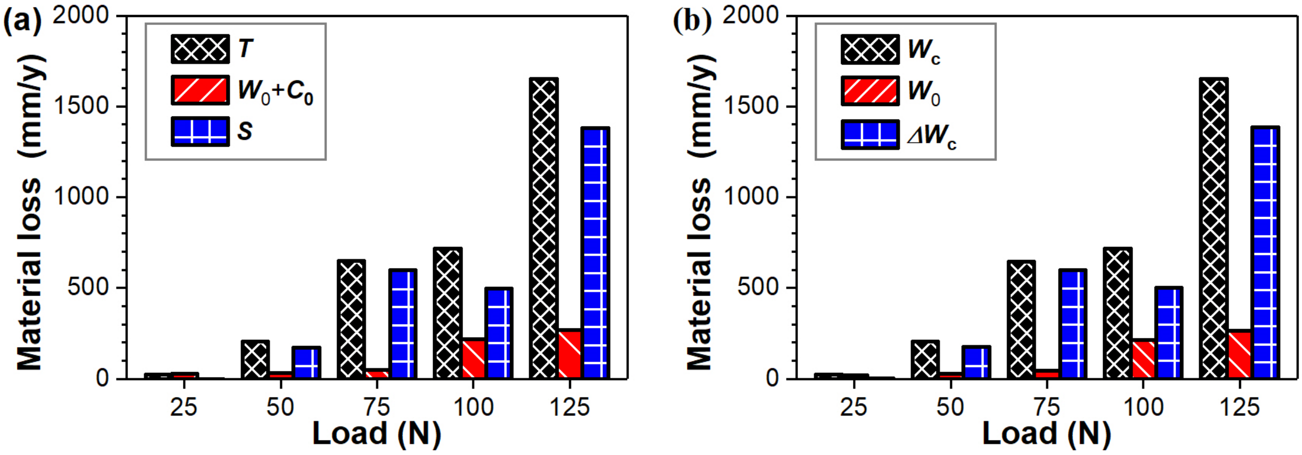

Figure 4. (**a**) The contribution of wear (W_0), corrosion (C_0) and wear–corrosion synergy (S) to the total material loss rate (T) and (**b**) total wear rate (W_c), mechanical wear rate (W_0) and the change in the mechanical wear rate due to corrosion (ΔW_c) of 40Cr15Mo2VN under different applied loads in acetic acid solution with a pH value of 3.

3.3. Electrochemical Tests

Figure 5a shows the open-circuit potential of the 40Cr15Mo2VN alloy under different applied loads. As 40Cr15Mo2VN was exposed to acetic acid, the corrosion potential shifted toward the positive direction, indicating that the 40Cr15Mo2VN alloy has a strong passivation ability. The passive tread terminated immediately after the sliding process began and rapidly reached the balance between passivation and wear of the formed passive film, showing a constant value of corrosion potential during sliding. As the applied load increased from 25 N to 125 N, the corrosion potential decreased from −0.49 V to −0.54 V, which is closely related to the degraded corrosion resistance at higher loads. Figure 5b shows the potentiodynamic polarization curves of 40Cr15Mo2VN at various loads, and the E_{corr} and i_{corr} determined by fitting the potentiodynamic polarization curves are listed in Table 2. The applied load had a considerable effect on E_{corr}, which was −0.418 V before sliding and gradually decreased from −0.471 V at 25 N to −0.548 V at 125 N during sliding with increasing load. The increasing i_{corr} shows that the passive films formed under higher loads had lower stability. When the applied load increased to 125 N, the value of i_{corr}

significantly increased, being approximately 100 times higher than that at 25 N. These observations demonstrate that corrosion damage is exacerbated at higher loads.

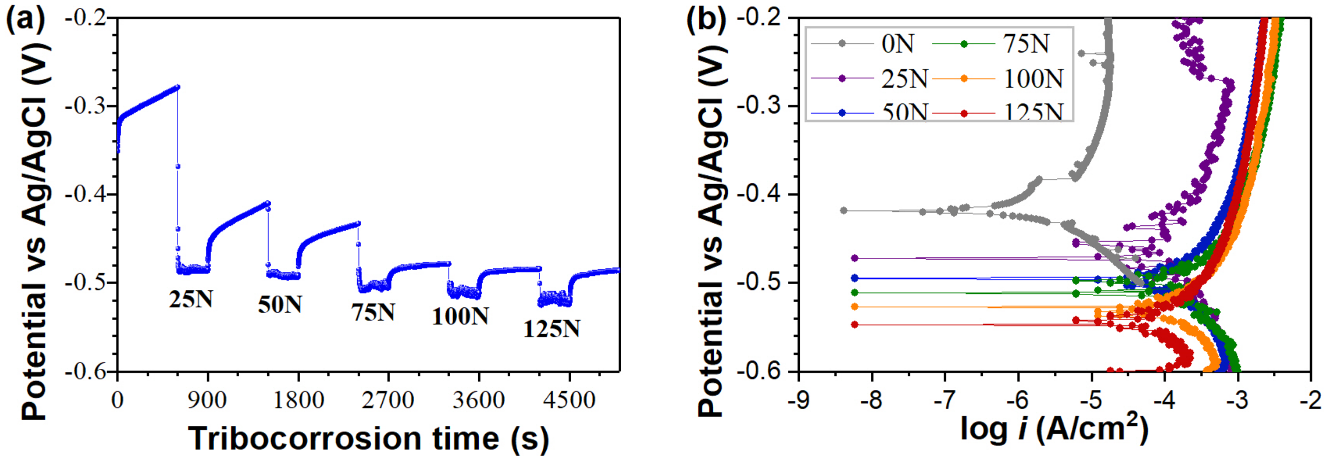

Figure 5. (**a**) Open-circuit potential (OCP) curves and (**b**) Tafel polarization curves of 40Cr15Mo2VN under different applied loads in acetic acid solution with a pH value of 3.

Table 2. Corrosion potential and corrosion current density of 40Cr15Mo2VN under different applied loads in acetic acid solution with a pH value of 3.

Load(N)	0	25	50	75	100	125
E_{corr} (V)	−0.418	−0.471	−0.494	−0.511	−0.527	−0.548
i_{corr} (µA/cm^2)	3.6	64.6	114.8	134.9	229.1	363.1

Sufficient studies have been conducted to interpret the tribocorrosion mechanisms of stainless steels in the presence of acetic acid. The material loss of 40Cr15Mo2VN induced by corrosion in acetic acid with a relatively low pH value of 3.0 was due to iron dissolution, which is expressed as shown in Equation (6) [30,31].

$$\mathrm{Fe} - 2\mathrm{e}^- \rightarrow \mathrm{Fe}^{2+} \tag{6}$$

The anodic iron dissolution was accompanied by two parallel cathodic reactions, namely, hydrogen ion reduction and the direct reduction of the undissociated acetic acid, which are shown in Equations (7) and (8) [27,32].

$$2\mathrm{H}^+ + 2\mathrm{e}^- \rightarrow \mathrm{H}_2 \tag{7}$$

$$2\mathrm{HAc} + 2\mathrm{e}^- \rightarrow \mathrm{H}_2 + 2\mathrm{Ac}^- \tag{8}$$

3.4. Damage Surface Morphologies

Figure 6 shows the typical damage morphology of the 40Cr15Mo2VN alloy under both tribocorrosion and mechanical wear conditions. The damage mechanism of material loss of 40Cr15Mo2VN was delamination of the metallic matrix, which became more prominent with increasing load. The damage induced by tribocorrosion was much more severe than that induced by mechanical wear, which is consistent with the previously determined higher material loss. The corrosion of acetic acid leads to higher wear due to dissolution of the surface layer, causing a rougher surface and thus making it easier to remove under the continual shear of the ceramic counterpart.

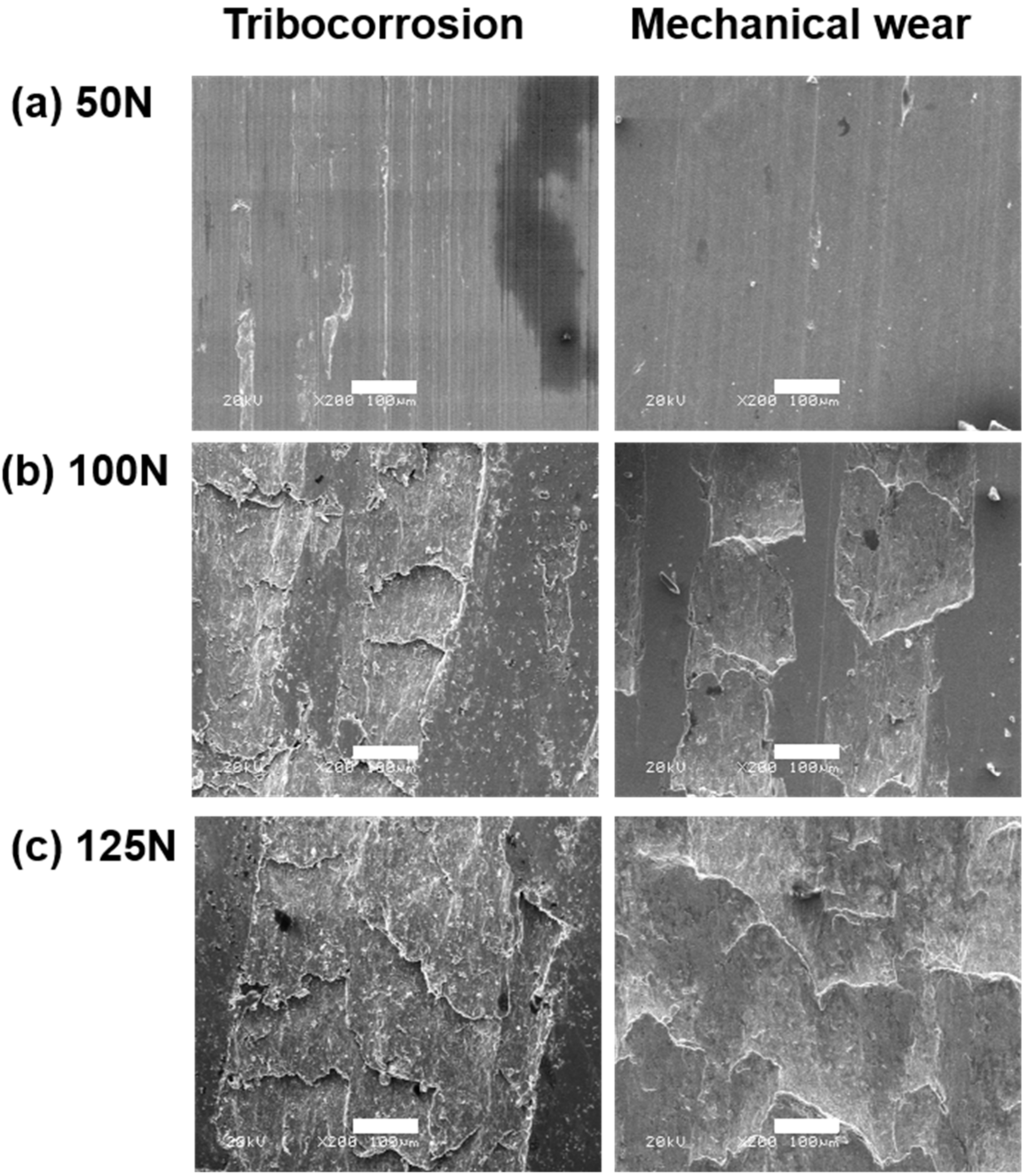

Figure 6. Typical morphologies of damaged surfaces of 40Cr15Mo2VN under different applied loads of 50 N, 100 N and 125 N.

Figure 7 displays the corresponding worn surfaces of the Si_3N_4 ceramic counterparts. In both tribocorrosion and mechanical wear conditions, ploughs and furrows parallel to the sliding direction were observed on the worn counterfaces, which was caused by the sliding between the asperities of 40Cr15Mo2VN and its ceramic counterpart. This indicates abrasive wear in the principal damage mechanism with or without the corrosive medium. At higher applied loads, the abrasive wear became more severe, being characterized by a larger wear area and deeper grooves in the microscopic view. Compared with mechanical wear, the damage induced by the combined effect of wear and corrosion was more prominent, possibly due to the contact surfaces of 40Cr15Mo2VN, which were roughened by corrosion, further leading to the acceleration of abrasive wear. Meanwhile, it can be seen that the ceramic counterpart was patched with adhered or transferred 40Cr15Mo2VN composed of many small clumps that had gathered during continuous sliding friction, which was sheared from 40Cr15Mo2VN by the asperities of the harder Si_3N_4 ceramic counterpart.

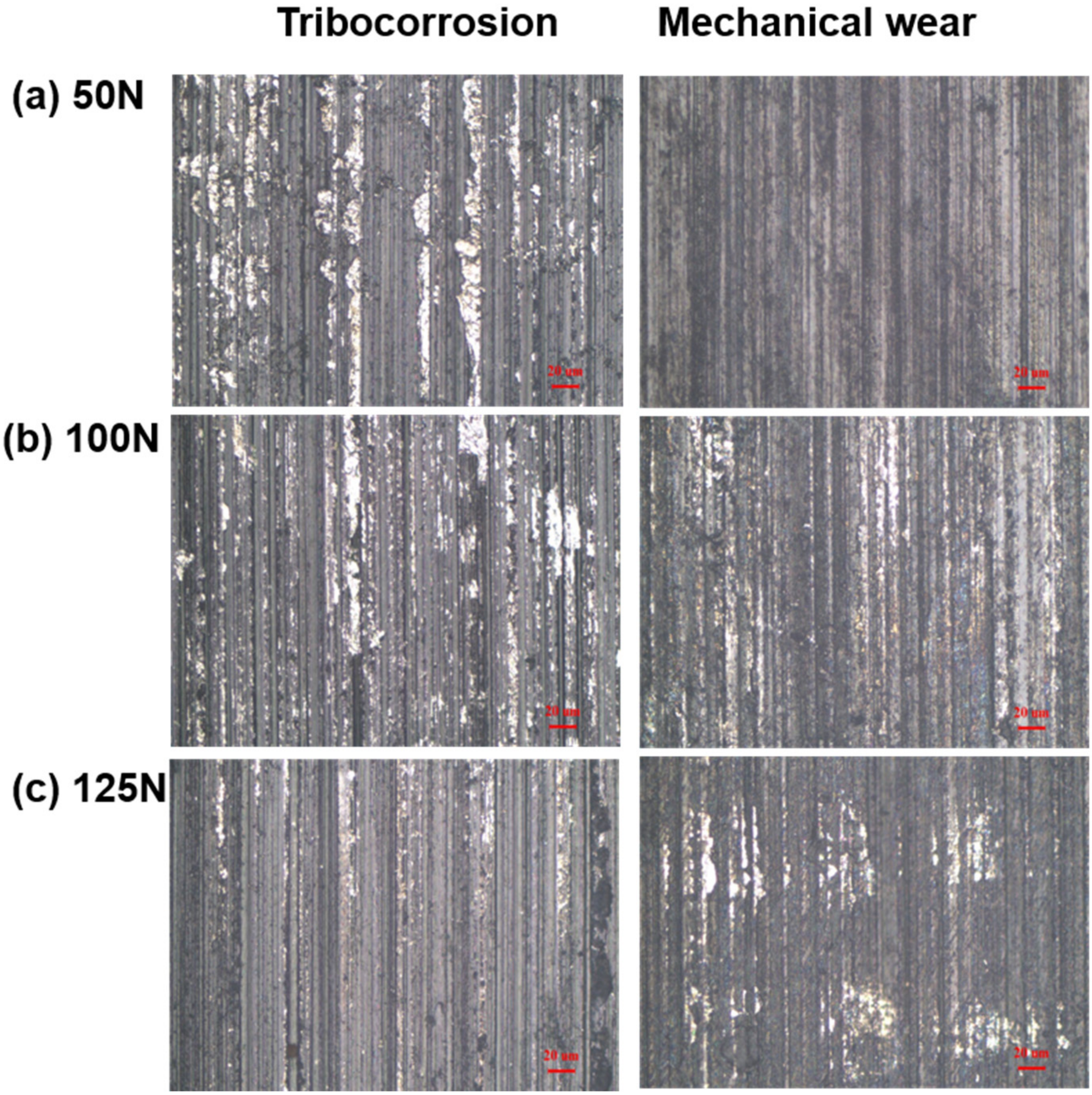

Figure 7. Typical morphologies of Si_3N_4 ceramic counterfaces under different applied loads of 50 N, 100 N and 125 N.

The typical wear debris is shown in Figure 8. On a morphological level, it was revealed that the wear debris generated under both tribocorrosion and mechanical wear was in the form of laminar flakes with different scales ranging from several microns to several hundred microns, depending on the applied load. Corrosion also influenced the morphology of wear debris, generating much finer and looser detached particles during tribocorrosion under the same load. It seems that the detached debris, due to wear, was removed from the contact area immediately after the contact between the metallic surface and the hard ceramic counterface, implying that the surface damage was primarily induced by the combined effect of chemical corrosion and mechanical wear. In other words, the removal of wear debris prevents the formation of a third body that further abrades the metallic surfaces and generates secondary damage as plows and furrows. As the applied load increases, increasing the ability of the pins to jackknife into the metal, when the rotation begins, plastic flow of the metal occurs, changing from furrow wear to spalling wear.

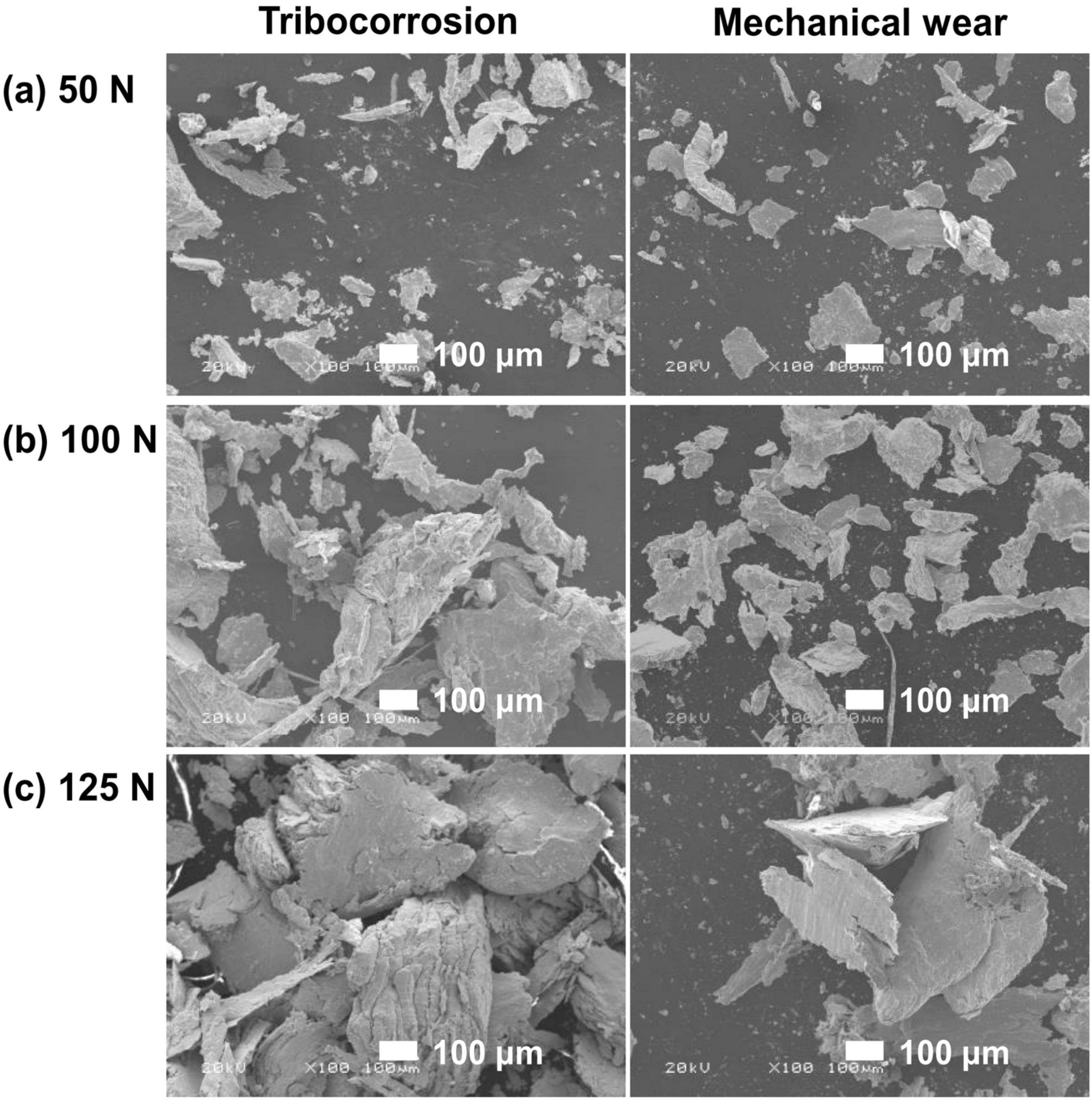

Figure 8. Typical morphologies of wear debris of 40Cr15Mo2VN under different applied loads of 50 N, 100 N and 125 N.

4. Conclusions

The tribocorrosion behavior of high-nitrogen stainless-steel 40Cr15Mo2VN under different loads in acetic acid solution with a pH of 3.0 was investigated in this study. The components of mechanical wear, corrosion and wear–corrosion interaction were quantitatively determined. The aim of this study was to develop engineering applications of nickel-free high-nitrogen steels, such as bearings, shafts and gears, in corrosive environments. However, the microstructural evolution and damage mechanisms under both tribocorrosion and mechanical wear and under different corrosive environments are not clear and need more investigation. The main conclusions of this work are presented below:

1. A positive synergy between corrosion and wear was quantitatively determined. Simultaneous corrosion significantly promoted mechanical wear during the tribocorrosion process.
2. The material loss induced by the tribocorrosion process in acetic acid solution primarily consisted of mechanical wear and corrosion-accelerated wear. The contribution of corrosion–wear synergism increased from approximately 6% at 25 N to over 83% at the highest load of 125 N.
3. The material loss induced by mechanical wear increased with increasing load. The failure of 40Cr15Mo2VN was dominated by typical delamination wear.
4. The corrosion mechanism of 40Cr15Mo2VN in acetic acid solution was mainly induced by general anodic dissolution, which promotes wear damage at surfaces.

Author Contributions: Q.S.: Data analysis, Writing—Original Draft Preparation and Resources; X.W.: Visualization, Data Curation, Formal Analysis and Writing—Original Draft Preparation; H.W.: Investigation, Date Curation and Methodology; Y.H.: Resources and Date Curation; Y.W.: Conceptualization, Writing—Review and Editing, Supervision, Resources; Z.L.: Validation, Supervision, Validation, Resources. All authors have read and agreed to the published version of the manuscript.

Funding: This work was financially supported by The National Key Research and Development Program of China (Grant No. 2021YFB3400400), the National Natural Science Foundation of China (Grant No. 21968032) and the Basic Research Fund of Central Universities (Grant No. 31920220044).

Data Availability Statement: The raw/processed data required to reproduce these findings cannot be shared at this time, as the data also form part of an ongoing study.

Conflicts of Interest: The authors declare no conflict of interest.

References

1. Davies, D.P. Survey of Fatigue Failures in Helicopter Components and Some Lessons Learnt. *Eng. Fail. Anal.* **2013**, *32*, 134–151. [CrossRef]
2. Bayoumi, F.M.; Ghanem, W.A. Effect of Nitrogen on the Corrosion Behavior of Austenitic Stainless Steel in Chloride Solutions. *Mater. Lett.* **2005**, *59*, 3311–3314. [CrossRef]
3. Berns, H. Manutacture and Application of High Nitrogen Steels. *ISIJ Int.* **1996**, *36*, 909–914. [CrossRef]
4. Al-Shelkamy, S.A.; Abu Hashish, H.M.; Mahdy, A.A. Structural and Tribological Properties of Heat-Treated Stainless Steels against Abrasive and Lubricant Wear Conditions. *Coatings* **2021**, *11*, 1473. [CrossRef]
5. Qiao, Y. Effect of Aging Treatment on Microstructure and Corrosion Behavior of a Fe-18Cr-15Mn-0.66N Stainless Steel. *J. Mater. Sci.* **2022**, *107*, 197–206. [CrossRef]
6. Abreu, D.; Silva, W.M., Jr.; Ardila, M.A.N.; De Mello, J.D.B. Tribocorrosion in Ferritic Stainless Steels: An Improved Methodological Approach. *Mat. Res.* **2022**, *25*, e20210179. [CrossRef]
7. Sastry, S.D.; Rohatgi, P.K.; Abraham, K.P.; Prasad, Y.V.R.K. Influence of Heat Treatment on the Strength and Fracture Behaviour of Fe-12Cr-6Al Ferritic Stainless Steel. *J. Mater. Sci.* **1982**, *17*, 3009–3016. [CrossRef]
8. Reed, R.P. Nitrogen in Austenitic Stainless Steels. *JOM* **1989**, *41*, 16–21. [CrossRef]
9. Simmons, J.W. Overview: High-Nitrogen Alloying of Stainless Steels. *Mater. Sci. Eng. A* **1996**, *207*, 159–169. [CrossRef]
10. Metikoš-Hukovic, M.; Babic, R.; Grubač, Z.; Petrovic, Z.; Lajçi, N. High Corrosion Resistance of Austenitic Stainless Steel Alloyed with Nitrogen in an Acid Solution. *Corros. Sci.* **2011**, *53*, 2176–2183. [CrossRef]
11. Pujar, M.G. Electrochemical Noise Studies of the Effect of Nitrogen on Pitting Corrosion Resistance of High Nitrogen Austenitic Stainless Steels. *Corros. Sci.* **2011**, *53*, 4178–4186. [CrossRef]
12. Xia, L.; Li, H.; Feng, H.; Jiang, Z.; Zhu, H.; Zhang, S.; Wang, X. Enhanced Strength and Toughness of High Nitrogen Stainless Bearing Steel by Controlling Interstitial Partitioning via V-Microalloying. *J. Mater. Sci. Technol.* **2023**, *151*, 204–218. [CrossRef]

13. Gavriljuk, V. On the Correlation between Electron Structure and Short Range Atomic Order in Iron-Based Alloys. *Acta Mater.* **2000**, *48*, 3879–3893. [CrossRef]
14. Gavriljuk, V.G.; Shanina, B.D.; Berns, H. A Physical Concept for Alloying Steels with Carbon + nitrogen. *Mater. Sci. Eng. A* **2008**, *481–482*, 707–712. [CrossRef]
15. Feng, H.; Li, H.-B.; Jiang, Z.-H.; Zhang, T.; Dong, N.; Zhang, S.-C.; Han, P.-D.; Zhao, S.; Chen, Z.-G. Designing for High Corrosion-Resistant High Nitrogen Martensitic Stainless Steel Based on DFT Calculation and Pressurized Metallurgy Method. *Corros. Sci.* **2019**, *158*, 108081. [CrossRef]
16. Wang, Q.; Zhang, B.; Ren, Y.; Yang, K. Eliminating Detrimental Effect of Cold Working on Pitting Corrosion Resistance in High Nitrogen Austenitic Stainless Steels. *Corros. Sci.* **2017**, *123*, 351–355. [CrossRef]
17. Cheng, H.; Luo, H.; Wang, X.; Pan, Z.; Jiang, Y.; Li, X. Electrochemical Corrosion and Passive Behavior of a New High-Nitrogen Austenitic Stainless Steel in Chloride Environment. *Mater. Chem. Phys.* **2022**, *292*, 126837. [CrossRef]
18. Clayton, C.R.; Halada, G.P.; Kearns, J.R. Passivity of High-Nitrogen Stainless Alloys: The Role of Metal Oxyanions and Salt Films. *Mater. Sci. Eng. A* **1995**, *198*, 135–144. [CrossRef]
19. Olefjord, I.; Wegrelius, L. The Influence of Nitrogen on the Passivation of Stainless Steels. *Corros. Sci.* **1996**, *38*, 1203–1220. [CrossRef]
20. Qiao, Y.X.; Zheng, Y.G.; Okafor, P.C.; Ke, W. Electrochemical Behaviour of High Nitrogen Bearing Stainless Steel in Acidic Chloride Solution: Effects of Oxygen, Acid Concentration and Surface Roughness. *Electrochim. Acta* **2009**, *54*, 2298–2304. [CrossRef]
21. Zhu, Y.; Ning, L.; Liu, E.; Zhou, Y.; Tan, Z.; Tong, J.; Li, H.; Zheng, Z. A Novel Precipitation Mechanism of Laves Phase in Fe-30Cr-2Mo Super Ferritic Stainless Steel: In-Situ Phase Transformation. *Mater. Lett.* **2023**, *338*, 134022. [CrossRef]
22. Zhu, Y.; Liu, H.; Wang, J.; Yan, F. Antagonistic Effect of Electrochemical Corrosion on the Mechanical Wear of Monel 400 Alloy in Seawater. *Corros. Sci.* **2022**, *198*, 110120. [CrossRef]
23. Zhang, B.; Wang, J.; Yan, F. Load-Dependent Tribocorrosion Behaviour of Nickel-Aluminium Bronze in Artificial Seawater. *Corros. Sci.* **2018**, *131*, 252–263. [CrossRef]
24. Liu, M.; Duan, D.-L.; Jiang, S.-L.; Li, M.-Y.; Li, S. Tribocorrosion Behavior of 304 Stainless Steel in 0.5 Mol/L Sulfuric Acid. *Acta Metall. Sin. (Engl. Lett.)* **2018**, *31*, 1049–1058. [CrossRef]
25. Maher, M.; Iraola-Arregui, I.; Ben Youcef, H.; Rhouta, B.; Trabadelo, V. The Synergistic Effect of Wear-Corrosion in Stainless Steels: A Review. *Mater. Today Proc.* **2022**, *51*, 1975–1990. [CrossRef]
26. Chai, G.; Forsman, T.; Gustavsson, F.; Wang, C. Formation of Fine Grained Area in Martensitic Steel during Very High Cycle Fatigue: Formation of Fine Grained Area in Martensitic Steel during Very High Cycle Fatigue. *Fatigue Fract. Eng. Mater. Struct.* **2015**, *38*, 1315–1323. [CrossRef]
27. Li, S.; Zhang, C.; Lu, J.; Chen, R.; Chen, D.; Cui, G. A Review of Progress on High Nitrogen Austenitic Stainless-Steel Research. *Mater. Express* **2021**, *11*, 1901–1925. [CrossRef]
28. Shen, H. Effects of Nitrogen on Predominant Sintering Mechanism during the Initial Stage of High Nitrogen Nickel-Free Stainless Steel Powder. *J. Alloys Compd.* **2023**, *945*, 169230. [CrossRef]
29. Zhou, R.; Northwood, D.O.; Liu, C. On Nitrogen Diffusion during Solution Treatment in a High Nitrogen Austenitic Stainless Steel. *J. Mater. Res. Technol.* **2020**, *9*, 2331–2337. [CrossRef]
30. Singh, M.M.; Gupta, A. Corrosion Behavior of Mild Steel in Acetic Acid Solutions. *Corrosion* **2000**, *56*, 371–379. [CrossRef]
31. Kahyarian, A. Acidic Corrosion of Mild Steel in the Presence of Acetic Acid: Mechanism and Prediction. *Electrochim. Acta* **2017**, *258*, 639–652. [CrossRef]
32. Sutthiruangwong, S.; Wongpaiboon, C.; Sritha, N.; Anukulkich, N. Pitting Potential Improvement of 304 Stainless Steel in Hydrochloric Acid Solution by *Terminalia bellirica* Fruit Extract. *Metals* **2023**, *13*, 262. [CrossRef]